





## Terahertz photoconductivity and photocarrier dynamics in graphene–mesoporous silicon nanocomposites

Défi Junior Jubgang Fandio <sup>1,2,3,4,\*</sup>, Stéphanie Sauze <sup>2,3</sup>, Abderraouf Boucherif,<sup>2,3</sup> Richard Arès,<sup>2,3</sup> Bouraoui Ilahi <sup>2,3,4</sup> and Denis Morris <sup>1,2,3,4</sup>

<sup>1</sup>*Département de Physique, Regroupement Québécois sur les Matériaux de Pointe, Université de Sherbrooke, 2500 Boulevard Université, Sherbrooke, Québec, Canada J1K 2R1*

<sup>2</sup>*Laboratoire Nanotechnologies Nanosystèmes (LN2), CNRS UMI-3463, Institut Interdisciplinaire d'Innovation Technologique (3IT), Université de Sherbrooke, 3000 Boulevard Université, Sherbrooke, Québec, Canada J1K 0A5*

<sup>3</sup>*Institut Interdisciplinaire d'Innovation Technologique (3IT), Université de Sherbrooke, 3000 Boulevard Université, Sherbrooke, Québec, Canada J1K 0A5*

<sup>4</sup>*Institut Quantique, Université de Sherbrooke, 2500 Boulevard Université, Sherbrooke, Québec, Canada J1K 2R1*



(Received 14 May 2020; revised 18 August 2020; accepted 19 August 2020; published 9 September 2020)

We investigate charge transport and photocarrier dynamics in graphene–mesoporous silicon nanocomposites using optical-pump terahertz-probe measurements. The nanocomposite material consists of a free-standing mesoporous silicon membrane whose specific surface is coated with a few-layer graphene shell. Temporal decays of the differential transmission measurements are reproduced using a biexponential function with an initial decay time of 5 ps and a longer decay time of about 25 ps. These decay times are significantly reduced compared to the values of  $\tau_1 \sim 74$  ps and  $\tau_2 \sim 730$  ps obtained for the uncoated mesoporous silicon membrane and this is attributed to the introduction of additional surface defects formed during the graphene deposition process. Based on the influence of the laser fluence on the time-resolved differential transmission curves, a capture/recombination model is proposed to describe the photocarrier dynamics in these nanocomposite materials. Frequency-dependent complex photoconductivity data curves are extracted from the terahertz waveforms taken at different optical-pump THz-probe delays. These data curves are well reproduced using a modified Drude-Smith model taking into account diffusive-restoring currents. The  $c$  parameter of this model, which describes the degree of carrier localization, is about  $-0.73$  for the uncoated porous Si membrane and is approaching  $-1$  for graphene–mesoporous Si nanocomposites formed at temperatures above  $800^\circ\text{C}$ . For all the nanocomposites, the characteristics of the photoconductive material, in terms of photocarrier capture/recombination time and effective mobility, are of interest for the fabrication of pulsed terahertz devices.

DOI: [10.1103/PhysRevB.102.115407](https://doi.org/10.1103/PhysRevB.102.115407)

### I. INTRODUCTION

Porous silicon exhibits unique optoelectronic properties that have been very attractive for a broad range of applications over the last decades [1]. The possibility to form surface-to-volume ratios as large as  $1000\text{ m}^2/\text{cm}^3$  offers great interests in optical sensing and waveguiding [2,3], bio- and chemical sensing [4,5], as well as energy harvesting and conversion [4,6,7] applications. Quantum confinement of photocarriers introduces new interesting features including tunable luminescence over the whole visible spectrum, light trapping, and light modulation [8,9].

The optoelectronic properties of porous silicon depend crucially upon quantum confinement and on the surface chemistry of the silicon skeleton [1,9]. The size of the nanocrystallites and the presence of surface defects affect both the energy of the emitted photons and the efficiency of the radiative recombination channel [9–11]. Quantum confinement is directly related to the nanometric size of the silicon crystallites and can be engineered accordingly during

the fabrication process. On the other hand, different passivation treatments have been developed to minimize the influence of surface states on charge transport and photocarrier capture/recombination mechanisms in porous silicon [7,12,13]. In this paper, we are specifically interested in a surface treatment, developed within our group, that consists of the deposition of a few-layer graphenelike coating. The treated silicon mesoporous free-standing membranes showed better thermal and mechanical stability [14,15]. However, the influence of the graphene deposition conditions on the dynamics of carrier photoinjected into the Si nanocrystallites has not yet been studied.

Indeed, charge transport and photocarrier dynamics studies have already been carried out on various disordered systems such as the array of semiconductor nanocrystals embedded in an insulating matrix [16–20], laterally coupled semiconductor quantum dots [21,22], dense arrays of misoriented semiconductor nanowires [23–28], and porous semiconductor films [7,29–32]. Moreover, ultrafast photocarrier transport, capture, and recombination mechanisms were studied using various time-resolved optical spectroscopy techniques including laser-induced grating spectroscopy [29,33], time-resolved photoluminescence [20,28,34], and time-resolved

\*Defi.Junior.Jubgang.Fandio@USherbrooke.ca

pump-probe techniques [16–19,23,24,27,31]. These studies investigated the influence of the structural parameters on the dominant photocarrier capture and recombination mechanisms. Various charge transport models have been suggested to explain pump-probe measurements on a large variety of complex mesoscopic systems. Accordingly, the surface plasmon model describes transport in nanostructures such as semiconductor nanowires where carriers are subjected to electrostatic restoring forces [23,25,35]. The restoring forces cause carriers to undergo harmonic oscillations in the opposite direction to the driven field, leading to a net negative imaginary part of the complex conductivity. Carriers transport in composite nanostructures can be studied under the contexts of the effective medium theories (EMTs), such as the Maxwell-Garnett and the Bruggeman approximations [36,37]. These theories model the microscopic conductivity of nanoscale inclusions within a host matrix as they take into account the filling fraction, the shape, and the dielectric function of the inclusions. Monte Carlo simulations have shown to reliably describe charge transport in some semiconductor nanocrystals exhibiting weak carrier localization [38–40].

The Drude-Smith model is an extension of the classical Drude model that has successfully described a large variety of complex nanosystems including liquid metals [33], semiconductor nanowires [25,41,42], interconnected arrays of quantum dots [21,43], and multiphase semiconductor complexes [16–18,44]. In such systems, carriers undergo field-driven motion in the volume of the nanostructure with a discontinuous response when the carriers reach the nanoparticle boundaries. In spite of its success to accurately describe charge transport in many weakly confined systems, the Drude-Smith model has some criticism in that (i) no rigorous explanation is provided to justify the assumption of momentum persistence only after a single scattering event, and (ii) the definition of its fit parameters does not always provide insights beyond their phenomenological meaning. A recent work introduced an extended version of the Drude-Smith model that describes the physical shape of the low-frequency photoconductivity in terms of a diffusive-restoring current within the nanoparticle [38]. This diffusive-restoring current is caused by a photocarrier density gradient when an electric field modifies the profile of charge-carrier density within the nanoparticles.

Graphene–mesoporous silicon nanocomposites (GPSi-nCs) are an interesting system for these studies because they consist of an interconnected network of silicon nanocrystallites where charge transport can be affected by physical potential barriers at the semiconductor/insulator interfaces, by the presence of surface traps, and by charge accumulation effects at the boundaries of the nanocrystallites. Moreover, the effects of the graphenelike coating covering the nanocrystallites as well as the effects of the coating deposition temperature on the charge transport and photocarrier lifetime are exciting aspects to investigate in these nanomaterials.

In this context, time-resolved terahertz spectroscopy (TRTS) is used to probe charge-carrier transport and capture/recombination mechanisms in GPSi-nCs. The photocarrier dynamics was analyzed using a phenomenological model. Results show at least two decay times in the free-standing mesoporous silicon (mPSi) membrane and a

significant drop in their values in the GPSi-nCs. Extended analyses based on a set of rate equations were made to shed light on the nature of the capture/recombination dynamics in the nanocomposites. The study of the temporal evolution of the complex photoconductivity curves shows a good agreement between the experimental values and the fitting curves based on the modified Drude-Smith model described in Ref. [38]. Our results show that photocarrier lifetime can be adjusted with the graphenelike coating deposition temperature with preserved photocarrier mobility.

## II. EXPERIMENTS

The GPSi-nCs were fabricated from mPSi free-standing membranes. These membranes were prepared by electrochemical etching of a boron-doped (0.01–0.02  $\Omega$  cm) Si (100) substrate. The Si substrate was first dried under a nitrogen flow and placed into a single bath electrochemical cell filled with hydrofluoric acid (49%) and ethanol 1:1 (v/v). The mesoporous layer fabrication was carried out with a pulsed current density of 100 mA cm<sup>-2</sup> applied to the two electrodes in contact with the electrolyte. To detach the free-standing membrane from the Si substrate, the first electrolyte was replaced by a diluted solution of hydrofluoric acid (49%) and ethanol 1:3 (v/v) and a 220 mA cm<sup>-2</sup> pulsed current density was applied between the electrodes. The graphene deposition phase was achieved through chemical vapor infiltration (CVI). Initially, the mPSi free-standing membranes were put into a furnace and then purged with an argon-hydrogen gas mixture to prevent the formation of native oxides on the specific surface of the mesoporous silicon. Next, a continuous flux of argon, hydrogen, and acetylene was pumped into the furnace at 100 °C for 40 min. Finally, the temperature was raised to the graphene deposition temperature for 40 min. The nanocomposites studied in this work were synthesized at 750 °C (C750), 800 °C (C800), and 850 °C (C850). Typical images of a GPSi-nC (C750) were obtained using scanning electron microscopy (Zeiss LEO Supra 1530 VP microscope) as shown in Fig. 1. The samples' average thicknesses were estimated to 100  $\mu$ m.

The TRTS setup was coupled to a Ti:sapphire regenerative amplifier that delivers  $\sim$ 60 fs laser pulses centered at 800 nm with a 1 kHz repetition rate. The output laser beam was split into three beams: (i) a pump beam used to inject photocarriers in the Si nanocrystallites, (ii) an excitation beam used to generate the THz-probe beam, and (iii) a probing beam used to detect THz pulses transmitted through the samples. The THz-probe pulses were generated by optical rectification of the femtosecond laser pulses directed towards a 1-mm-thick ZnTe crystal and detected by electro-optic sampling using a 0.5-mm-thick ZnTe crystal. The optical pump and the THz pulses were linearly polarized and directed collinearly in the same direction at the sample surface. The optical-pump terahertz-probe (OPTP) measurements were obtained using two delay lines (one for the pump and the other for the probe beams). In the regime of low transient absorption, the pump-induced changes in the THz signal transmitted through the sample were obtained by chopping the pump (for time-resolved photoconductivity) and the probe (for frequency-resolved photoconductivity) at 455 Hz.

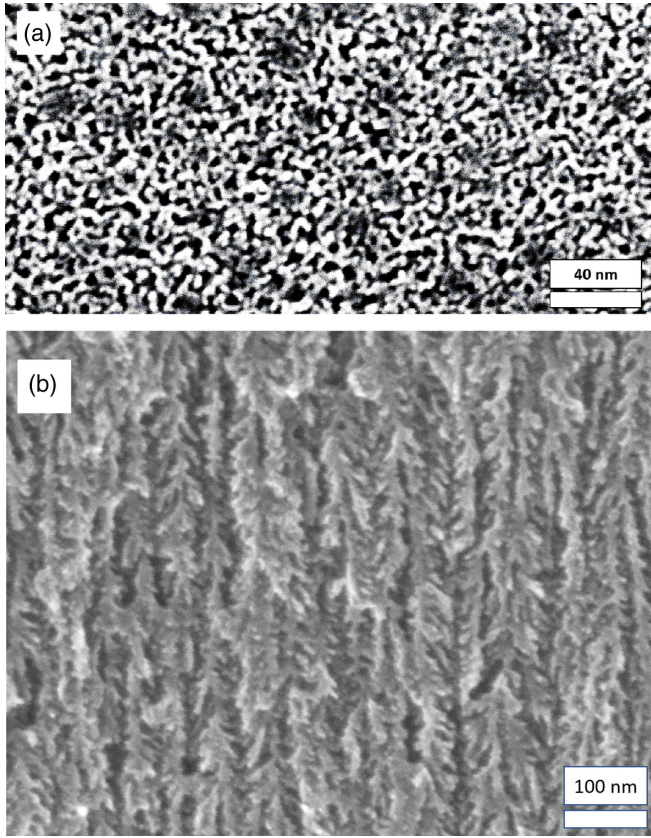


FIG. 1. Scanning electron microscopy (SEM) images: (a) In-plane and (b) cross-sectional views of the GPSi-nC prepared at 750 °C (C750).

All measurements were achieved in a dry environment, at room temperature (300 K).

### III. RESULTS AND DISCUSSION

#### A. Sample morphology

Figure 1 illustrates the in-plane and cross-sectional scanning electron micrographs of the C750 nanocomposite's sample. The in-plane view of SEM images illustrates a network of interconnected silicon nanocrystallites. The in-plane view shows that the structure consists of a network of Si nanocrystallites containing a high density of pores (black holes) randomly distributed over the entire surface. The cross-sectional view of the sample shows that the silicon nanocrystallites are elongated in the out-of-plane direction. Previous works have shown evidence of a graphenelike coating of these nanostructures with a preservation of their mPSi morphology during their fabrication process [14,15,45]. The average nanocrystallite size and pore diameters were estimated using IMAGEJ software to 6 and 17 nm, respectively. Moreover, the graphenelike coating thickness was shown to increase with the graphene deposition temperature [14,45].

#### B. Time-resolved photoconductivity

The density of surface traps in the porous material is such that the Si nanocrystallites are fully depleted: They contain no

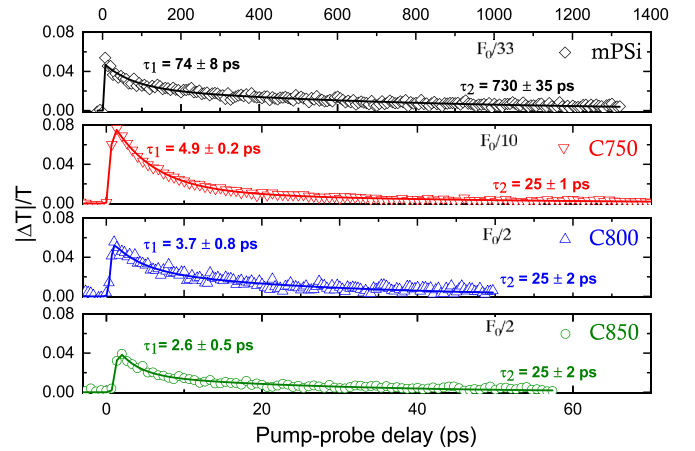


FIG. 2. OPTP measurements obtained for the free-standing mPSi and GPSi-nC samples. The value of the pump laser fluence is indicated in each graph, where  $F_0 = 3.4 \pm 0.9 \text{ mJ cm}^{-2}$ . Solid lines correspond to fits using Eq. (2).

free charges. Optical pumping of porous silicon can promote carriers into the Si conduction band. Pump-induced changes in the transmission of the THz beam were measured at the peak of the transmitted THz pulse. The differential pump-induced change in the transmitted signal, defined as

$$\Delta T/T = (T_{\text{pump}} - T_{\text{w/o pump}})/T_{\text{w/o pump}}, \quad (1)$$

is modified with the pump-probe delay. In the regime of low carrier absorption, we can consider that the time-dependent differential signal  $\Delta T(t)/T$  is proportional to the transient photoconductivity  $\Delta\sigma(t)$ . The  $\Delta\sigma(t)$  depends upon the change in the density of photocarriers  $\Delta n(t)$  (electrons and holes) in the Si nanocrystallites. In order to simplify the analysis, we consider that the signal is mainly governed by one type of carriers, even if the electron mobility is  $\sim 3$  times larger than the hole mobility in bulk Si. Moreover, after a fast relaxation time of typically a few hundreds of femtoseconds, the carrier mobility can often be considered a time-independent quantity. Therefore, the photoconductivity change can be expressed as  $\Delta\sigma(t) = e\mu\Delta n(t)$ , where  $\mu$  is the average photocarrier mobility.

Figure 2 depicts the OPTP measurements obtained for the free-standing mPSi and GPSi-nC samples. The laser fluence was adjusted for each sample such that the maximum differential transmission value is  $< 10\%$  to ensure linearity between  $\Delta T(t)/T$  and  $\Delta\sigma(t)$ . The experimental data curves were fitted with the well-known phenomenological model [23,31]

$$\frac{|\Delta T(t)|}{T} = \text{erfc}\left(\frac{-t}{\tau_r}\right) \left[ a_1 \exp\left(\frac{-t}{\tau_1}\right) + a_2 \exp\left(\frac{-t}{\tau_2}\right) \right], \quad (2)$$

where  $\tau_1$  and  $\tau_2$  are two characteristic decay times,  $a_1$  and  $a_2$  are their corresponding weights, and  $\tau_r$  is the rise time which is related to ultrafast hot photocarrier relaxation time. We use the value of  $\tau_r \sim 0.4 \text{ ps}$  for all fitting curves. Considering the maximum laser fluence value  $F_0 = 3.4 \pm 0.9 \text{ mJ cm}^{-2}$  and the sample porosity  $p \sim 60\%$  [45], the initial photocarrier density was estimated to  $3.0 \pm 0.7 \times 10^{19} \text{ cm}^{-3}$ .

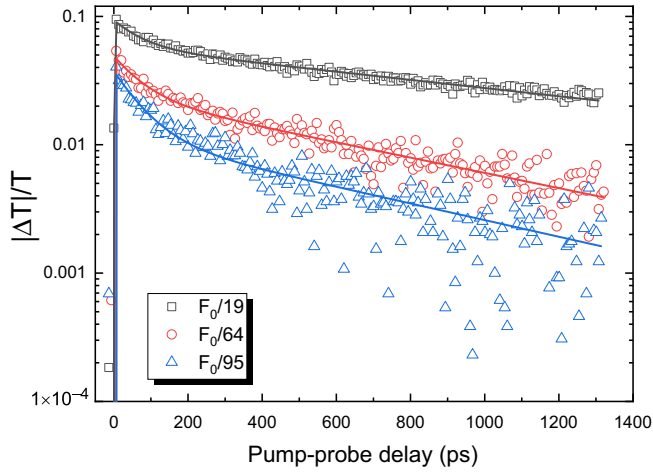


FIG. 3. OPTP measurements obtained for mPSi at three different laser fluence, where  $F_0 = 3.4 \pm 0.9 \text{ mJ cm}^{-2}$ . The solid lines represent the best fitting curves using Eq. (2).

The OPTP measurements obtained for three different laser fluences are shown in Figs. 3 and 4. For the mPSi sample, the best fitting curves using Eq. (2) are obtained for  $\tau_1 \sim 74 \pm 8 \text{ ps}$  and  $\tau_2 \sim 730 \pm 35 \text{ ps}$ . These decay times are significantly reduced to typically  $\tau_1$  of 2–5 ps range and  $\tau_2$  of about 25 ps for the GPSi-nCs. All fitting parameters are given in Table I. The decrease of the  $a_1/a_2$  ratio (from 2.2 to 0.6) with laser fluence indicates that some of these trap states are gradually being filled. The trapped photocarriers can be thermally reactivated and the overall photocarrier lifetime is limited by the slowest recombination process ( $\sim 730 \text{ ps}$  for the mPSi sample). For the GPSi-nC samples in Fig. 4, the faster exponential decay component dominates for all samples, and for all laser fluences ( $a_1/a_2 \gtrsim 1$ ). The exact photocarrier capture/recombination mechanisms are difficult to identify, but the drastic increase in the density of surface defects with the graphene deposition temperature certainly plays a key role in opening up different carrier capture/recombination channels. The relatively small influence of laser fluence on the dynamics of the OPTP signals is not compatible with the

TABLE I. Parameters obtained from the fits of the  $\Delta T(t)/T$  curves in Figs. 3 and 4 using Eq. (2). The maximum laser fluence is evaluated to  $F_0 = 3.6 \pm 0.9 \text{ mJ cm}^{-2}$ .

| Samples | Fluence<br>( $\mu\text{J cm}^{-2}$ ) | $\tau_1$<br>(ps) | $\tau_2$<br>(ps) | $a_1/a_2$       |
|---------|--------------------------------------|------------------|------------------|-----------------|
| mPSi    | $F_0/19$                             | $75 \pm 5$       | $1360 \pm 30$    | $0.62 \pm 0.01$ |
| mPSi    | $F_0/64$                             | $74 \pm 8$       | $730 \pm 35$     | $1.0 \pm 0.1$   |
| mPSi    | $F_0/95$                             | $75 \pm 8$       | $650 \pm 60$     | $2.2 \pm 0.2$   |
| C750    | $F_0/10$                             | $4.9 \pm 0.2$    | $25 \pm 1$       | $3.4 \pm 0.3$   |
| C750    | $F_0/19$                             | $4.8 \pm 0.3$    | $25 \pm 3$       | $4.8 \pm 0.8$   |
| C750    | $F_0/33$                             | $4.9 \pm 0.5$    | $25 \pm 8$       | $7 \pm 3$       |
| C800    | $F_0$                                | $4.9 \pm 0.5$    | $25 \pm 2$       | $1.4 \pm 0.1$   |
| C800    | $F_0/2$                              | $3.7 \pm 0.7$    | $25 \pm 2$       | $1.0 \pm 0.1$   |
| C800    | $F_0/3$                              | $2.0 \pm 0.6$    | $25 \pm 2$       | $0.9 \pm 0.1$   |
| C850    | $F_0$                                | $5.3 \pm 0.4$    | $25 \pm 2$       | $2.0 \pm 0.2$   |
| C850    | $F_0/2$                              | $2.6 \pm 0.5$    | $25 \pm 2$       | $1.6 \pm 0.1$   |
| C850    | $F_0/3$                              | $2.3 \pm 0.4$    | $25 \pm 3$       | $1.8 \pm 0.1$   |

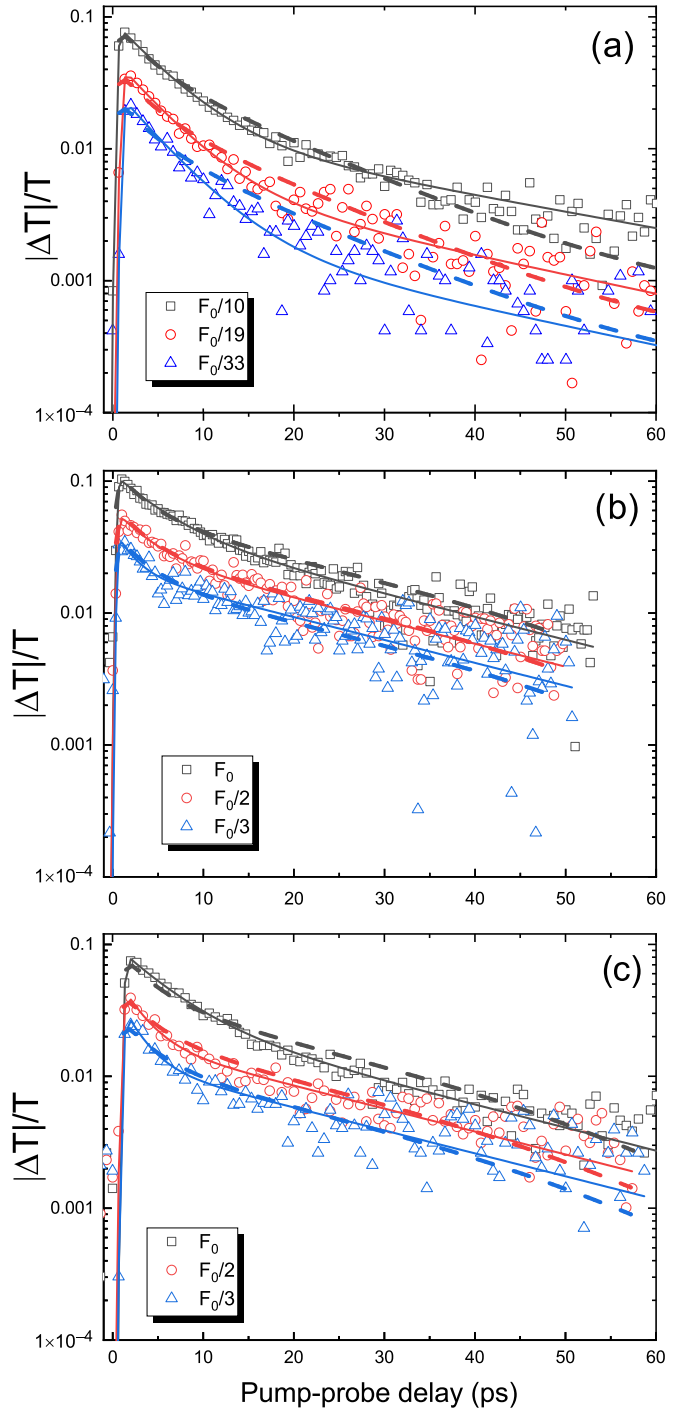


FIG. 4. OPTP measurements obtained for (a) C750, (b) C800, and (c) C850 samples, for different laser fluences, where  $F_0 = 3.4 \pm 0.9 \text{ mJ cm}^{-2}$ . The solid lines correspond to the best fitting curves using the biexponential decay function Eq. (2). The dotted lines represent the best fitting curves using the rate equations (3)–(5).

opening of an Auger-type recombination channel but rather suggests that the saturation limit of the various trap states is not reached at the highest laser fluence used for these experiments.

The role of the graphenelike coating on the photocarrier dynamics in GPSi-nCs resumes essentially in the creation of carbon-related defects at the Si/graphene interfaces [15].

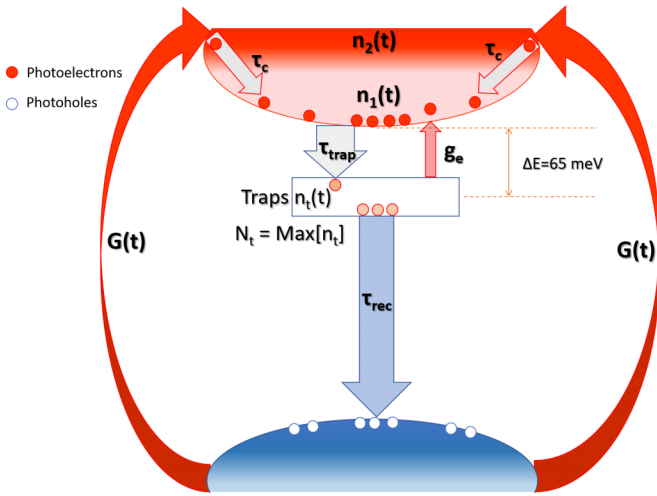


FIG. 5. Schematic of capture/recombination dynamics of GPSi-nCs as formulated using the system of rate equations (3)–(5).

Indeed, photocarriers can be injected into the graphenelike layer by the optical pump, but these should not contribute to the photoconductivity measurements obtained here for the following reasons. First, the graphenelike coating extends mainly in the direction transverse to the THz field so that transport in the direction parallel to the plane of the porous membrane is severely blocked. Second, previous studies have shown that the photocarrier relaxation/recombination dynamics in graphene is ultrafast, on the order of a few hundred femtoseconds [46–49]: The contribution of these photocarriers to the  $\Delta T(t)/T$  signals would thus be barely perceptible on the timescale of our experiments.

### C. Modeling the capture/recombination dynamics in GPSi-nCs

An in-depth analysis of the photocarrier dynamics can be made from a series of rate equations of the photocarrier populations occupying the different states relevant to the system under study. Figure 5 shows a diagram of the energy bands of Si nanocrystallites with the valence band, conduction band, and trap states located in the forbidden gap of the semiconductor. The different arrows in this diagram summarize the various mechanisms of generation, relaxation, capture, and recombination of the photocarriers that are taken into account in our model. If the photoconductivity signal is dictated by the density of the photoelectrons present at the bottom of the conduction band  $n_1(t)$ , the following set of rate equations can be solved numerically to obtain its time evolution [50],

$$\frac{dn_2(t)}{dt} = G(t) - \frac{n_2(t)}{\tau_c}, \quad (3)$$

$$\frac{dn_1(t)}{dt} = \frac{n_2(t)}{\tau_c} - \frac{n_1(t)}{\tau_{\text{trap}}} \left(1 - \frac{n_t}{N_t}\right) + g_e n_t, \quad (4)$$

$$\frac{dn_t(t)}{dt} = \frac{n_1(t)}{\tau_{\text{trap}}} \left(1 - \frac{n_t}{N_t}\right) - g_e n_t - \frac{n_t}{\tau_{\text{rec}}}, \quad (5)$$

where  $n_2(t)$  corresponds to the density of hot photoelectrons and  $n_{\text{trap}}(t)$  represents the density of trapped photoelectrons. The density of hot photoelectrons generated by a

Gaussian-like laser pulse is included in the term  $G(t)$ . The hot photoelectron relaxation time is designated by  $\tau_c$ . In this model, the photoelectrons at the bottom of the conduction band are mainly captured by trap states in a characteristic time  $\tau_{\text{trap}}$  and we take into account the filling of these states via the term  $N_t$  which corresponds to the total density of these traps. Equation (4) also includes a term for thermal reactivation of these trapped photocarriers via a generation rate ( $g_e$ ) which can be written as follows [50],

$$g_e = \frac{1}{\tau_{\text{trap}}} \frac{N_c}{N_t} \exp\left(-\frac{\Delta E}{k_B T}\right), \quad (6)$$

where  $\Delta E$  is the activation energy and  $N_c$  the effective density of states in the conduction band. For the effective electron density of state, we consider the bulk silicon value of  $N_c$  which is about  $3.2 \times 10^{19} \text{ cm}^{-3}$  at 300 K [51]. Finally, Eq. (5) includes a recombination term of the trapped photoelectrons with holes in the valence band, characterized by a time  $\tau_{\text{rec}}$  which governs the dynamics of the  $\Delta T(t)/T$  signals, at longer times.

The OPTP data curves shown in Fig. 4 are well reproduced by the set of rate equations (3)–(5) fitting curves (dotted), with a limited number of adjustable parameters. The best fits were obtained for shallow trap states located at  $\Delta E = 65 \text{ meV}$  for all the GPSi-nCs. The initial capture times are about  $\tau_{\text{trap}} = 4.3 \pm 0.3$ ,  $4.1 \pm 0.2$ , and  $4.0 \pm 0.1 \text{ ps}$ , for the C750, C800, and C850 samples, respectively. The corresponding recombination times of the trapped carriers are  $\tau_{\text{rec}} = 110 \pm 36$ ,  $100 \pm 26$ , and  $90 \pm 17 \text{ ps}$ . These capture and recombination times do not show any significant evolution with the graphene deposition temperature. However, the density of traps formed during the graphene deposition process seems to be the key parameter that governs the photocarrier dynamics in our nanocrystallites. The initial photocarrier densities deduced from the experimental pump fluence  $F_0/10$  and  $F_0/2$  used for our mPSi and C750 samples are  $3.0 \times 10^{18} \text{ cm}^{-3}$  and  $1.7 \times 10^{19} \text{ cm}^{-3}$ , respectively. These values are consistent with the values  $5.8 \times 10^{18} \text{ cm}^{-3}$  and  $2.0 \times 10^{19} \text{ cm}^{-3}$  obtained from the global fits of the  $\Delta T(t)/T$  data curve of these samples. Our results show that the density of the traps significantly increases from about  $N_t = 3.0 \pm 0.3 \times 10^{15} \text{ cm}^{-2}$  in C750 to  $2.1 \pm 0.2 \times 10^{16} \text{ cm}^{-2}$  in C800 and C850 samples.

### D. Frequency-dependent photoconductivity

The temporal evolution of the frequency-dependent photoconductivity is obtained from the pump-induced changes in the transmitted THz pulse measured at different pump-probe delays. Figure 6(a) shows the normalized  $\Delta T(t)/T$  signal obtained for the mPSi sample. Figure 6(b) shows the THz field transmitted through the sample with and without the optical pump, and measured at a fixed pump-probe delay where the photoconductivity reaches a maximum. Note that the signal is reduced in the presence of the optical pump because of the increased THz absorption due to the presence of extra photocarriers in the conduction bands of the Si nanocrystallites. The inset in Fig. 6(b) illustrates the Fourier amplitudes of the THz waveforms from which the frequency-dependent photoconductivity curves were extracted. By monitoring the delay between the pump and the probe pulses, it is also possible to

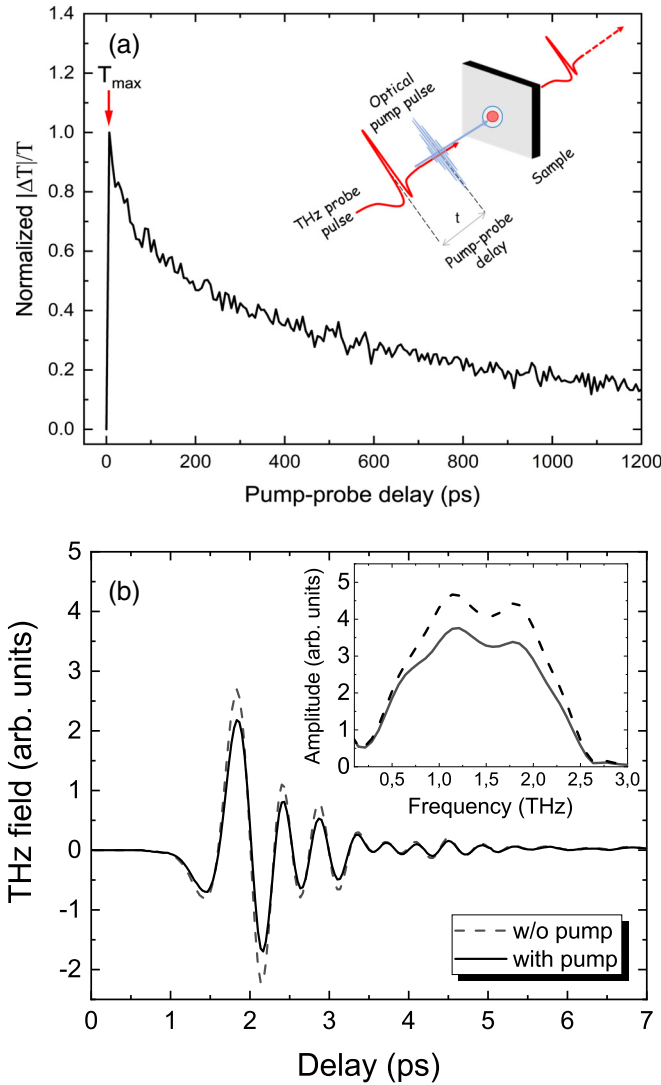


FIG. 6. (a) Normalized  $\Delta T(t)/T$  for mPSi. The inset depicts a schematic of the TRTS experiment. (b) Temporal shapes of THz pulses and their corresponding Fourier amplitudes in the inset.

derive the photoconductivity at different pump-probe delays. In systems where carriers are subject to weak localization, the photoconductivity can be described using the modified Drude-Smith formula [38]

$$\Delta\sigma(\omega) = \frac{Ne^2\tau'/m^*}{1 - i\omega\tau'} \left( 1 + \frac{c}{1 - i\omega/a} \right), \quad (7)$$

where  $e$  is the elementary charge,  $N$  is the excess photocarrier density,  $m^*$  is the effective mass, and  $c$ , often referred to as the *localization parameter*, can vary from 0 to  $-1$ .  $\tau'$  is the effective scattering time defined as

$$\tau' = \left( \frac{1}{\tau} + \frac{2Rv_{th}}{d} \right)^{-1}, \quad (8)$$

where  $\tau$  is the bulk scattering time,  $R$  is the nanocrystallite boundary reflection coefficient,  $d$  is the average nanocrystallite size, and  $v_{th}$  the photocarrier thermal velocity. The  $c$  parameter integrates the microscopic properties dictating the

frequency behavior of the real and imaginary parts of the photoconductivity at THz frequencies [38,39]. Charge carrier dynamics with  $c = -1$  corresponds to a full localization of the carrier within the nanocrystallites: This phenomenon is reflected by a total suppression of the real part of the photoconductivity at zero frequency as well as the appearance of a negative imaginary counterpart of this complex photoconductivity, at low frequencies. For  $c = 0$ , the scattering event is isotropic and we recover the classical Drude photoconductivity. In Eq. (7), the parameter  $a$  represents the diffusive-restoring current rate induced by the photocarrier density gradient at the boundaries of the nanocrystallites. It is defined as

$$a = \frac{12D'}{d^2} = \frac{12v_{th}^2\tau'}{d^2}, \quad (9)$$

where  $D'$  is the modified diffusion coefficient. Figure 7 illustrates the simultaneous fits of six  $\Delta\sigma(\omega)$  data curves using the modified Drude-Smith parameters  $N$ ,  $\tau'$ , and  $c$ , described in Eq. (7), for each sample. These data curves are the real and imaginary parts of  $\Delta\sigma(\omega)$  taken at three different pump-probe delays. In these fits, the photocarrier density  $N = N_0 \exp(-t/\tau_{decay})$  is assumed to decay exponentially from the total injected density  $N_0$  with an effective time  $\tau_{decay}$ . For the mPSi and C750 samples, the initial carrier density extracted from the fits in Fig. 7 using an effective mass  $m^* = 0.26m_0$  is  $N_0 = 4.1 \pm 0.1 \times 10^{18} \text{ cm}^{-3}$  and about  $1.1 \pm 0.4 \times 10^{18} \text{ cm}^{-3}$  for C800 and C850 samples. The photocarrier decay times extracted from this fitting procedure give  $\tau_{decay} = 80 \pm 1 \text{ ps}$  for mPSi,  $\tau_{decay} = 4.4 \pm 0.1 \text{ ps}$  for C750,  $\tau_{decay} = 2.9 \pm 0.1 \text{ ps}$  for C800, and  $\tau_{decay} = 2.4 \pm 0.1 \text{ ps}$  for C850 samples, respectively. These decay values are consistent with the values of the fast decay times associated with ultrafast capture by the surface trap states determined using the biexponential fitting values in Table I and are also similar to the  $\tau_{trap}$  values obtained from our capture/recombination model in GPSi-nCs.

A scattering time  $\tau' = 66 \pm 3 \text{ fs}$  and its corresponding effective mobility of  $\mu_{eff} = 446 \pm 20 \text{ cm}^2/(\text{V s})$  were found for all our samples. This result is consistent with previous findings that the graphenelike coating deposition process stabilizes mechanically the mesoporous structure [14]: Since no deformation of the nanocrystallite occurs during the growth, the transport dynamics of photocarriers within the nanocrystallite network should remain unchanged, and perhaps might be modified at the surface of the nanocrystallites. Therefore, the relatively high photocarrier mobility in the mPSi sample is preserved in GPSi-nCs despite the sharp rise in the trap states at the boundaries. This result is also consistent with the fact that diffusion at the nanocrystallites' boundaries has little effect on the scattering time  $\tau'$  as defined in Eq. (8).

The best fitting values for the *localization parameter* are  $c = -0.727 \pm 0.001$  for mPSi,  $c = -0.774 \pm 0.002$  for C750,  $c = -0.94 \pm 0.01$  for C800, and  $c = -0.956 \pm 0.004$  for C850 samples, respectively. The increase in  $|c|$  with the graphenelike coating deposition temperature is a good indication of the rise in photocarrier reflection at the nanocrystallites' boundaries since  $c$  is expected to increase exponentially with  $R$  as verified with Monte Carlo simulations [38]. Moreover, the photocarrier localization is found to be

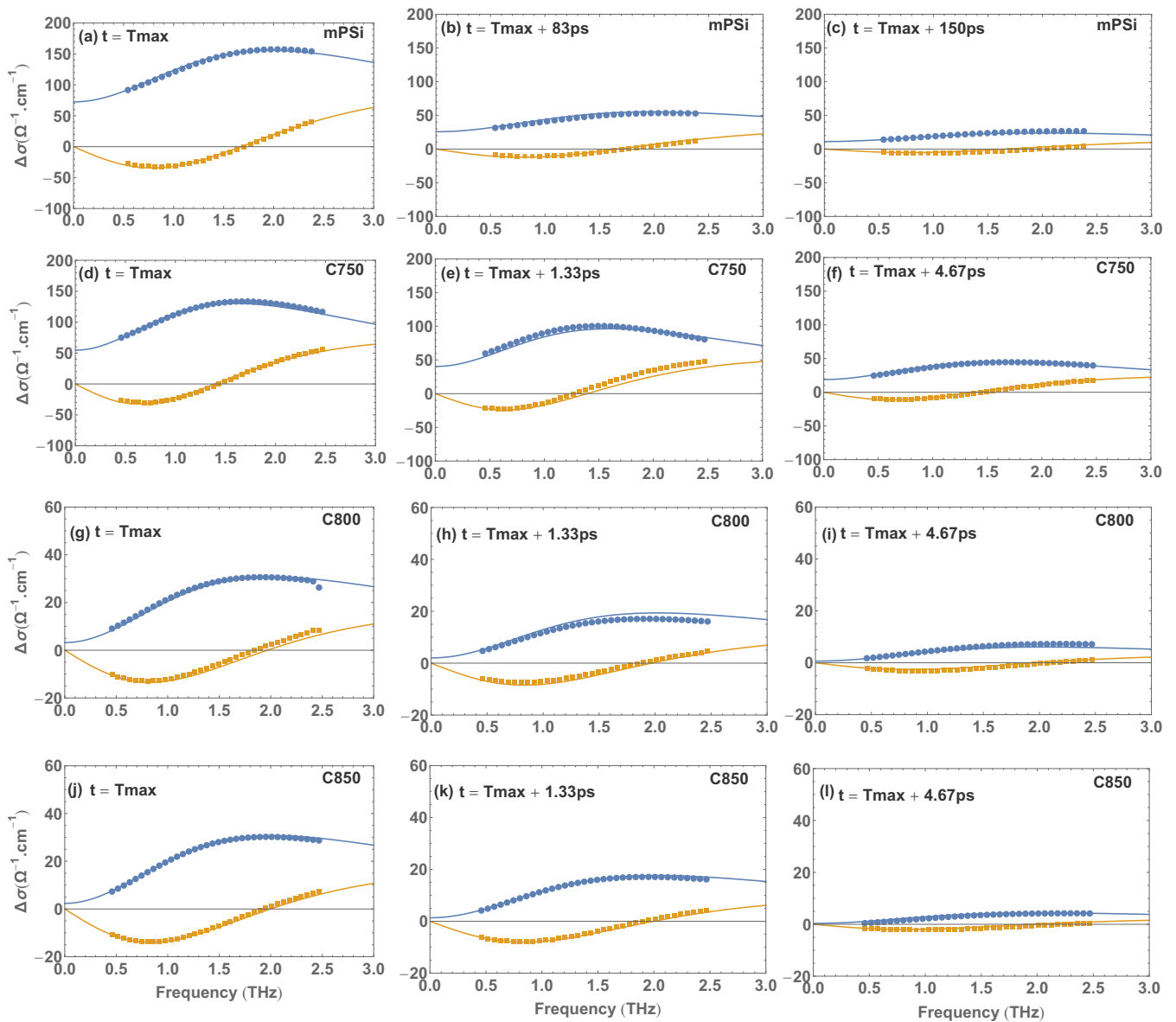


FIG. 7. Frequency-dependent photoconductivity  $\Delta\sigma(\omega)$  curves for the mPSi and GPSi-nC samples. The blue (orange) curves represent the real (imaginary) part of the photoconductivity. For each sample, all  $\Delta\sigma(\omega)$  curves at three pump-probe delays were simultaneously fitted using the modified Drude-Smith model [Eq. (7)] with the photocarrier density decreasing as  $N = N_0 \exp(-t/\tau_{\text{rec}})$ .

nearly constant [ $c(t) = c$ ] as a function of the pump-probe delay. This behavior differs from the time-varying localization phenomenon observed in other nanostructures such as Si nanocrystals embedded in a  $\sim 1.5$ -nm-thick  $\text{SiO}_2$  film [16,52]. In these structures, the time-varying long-range transport tracked by  $c(t)$  has been attributed to thermionic emissions [53], percolation hopping [52,54], and a Schottky-like potential at nanocrystal boundaries [16,53]. The Schottky-like potential arises as photocarriers get captured at interface states and ionize these states such that the barrier height is raised, resulting in the increase of the carrier backscattering probability. In our sample, the nearly time-independent  $c$  value could imply that the interface potential barrier height is not significantly affected by charge-carrier accumulation at the Si nanocrystallite boundaries. This argument is consistent

with the scenario where the maximum photocarrier density is significantly smaller than the density of traps  $N_t$  such that charge accumulation effects are negligible compared to the confining potential barrier. For the mPSi membrane, intergrain transport occurs via regions with a narrow potential barrier width where the nanocrystallites are almost in contact. The DC transport of photocarriers in the direction of the THz field could then be dominated by tunneling between these nanocrystallites. The graphene deposition at high temperature tends to promote the growth of a thin layer of carbon oxides or SiC all around the nanocrystallites [45], thus suppressing the intergrain connection regions that could remain in the mesoporous membrane. Si nanocrystallites are increasingly isolated from each other as the deposition temperature increases.

#### IV. CONCLUSIONS

In summary, we have investigated the ultrafast photocarrier dynamics and terahertz photoconductivity in GPSi-nCs using TRTS. Temporal decays of the OPTP measurements are reproduced using a biexponential function. The low and long decay time components are associated with the capture of the photocarriers by surface traps and then the recombination of the photocarriers within these traps. For the mPSi sample, the values of the decay times are  $\tau_1 \sim 74$  ps and  $\tau_2 \sim 730$  ps. Both decay times are significantly reduced for the GPSi-nCs, typically to  $\tau_1 \sim 5$  ps and  $\tau_2 \sim 25$  ps. An analysis of the photocarrier capture/recombination dynamics based on a rate equation model with saturable traps allows us to estimate the density of these traps in the GPSi nCs. The frequency-dependent photoconductivity of the GPSi-nCs and mPSi are well described by the modified Drude-Smith model

including diffusion-restoring currents. Our results show that the carrier mobility in mPSi is preserved for all our GPSi-nCs. The relatively high mobility and short photocarrier lifetimes found in GPSi-nCs make these nanocomposites very attractive candidates for pulsed terahertz applications.

#### ACKNOWLEDGMENTS

This work is financed by Natural Sciences and Engineering Research Council of Canada (NSERC), Canada Foundation for Innovation (CFI), and Fonds de recherche du Québec – Nature et Technologies (FRQNT). D.J.J.F. thanks O. Trépanier for valuable help in the numerical analysis of the  $\Delta T/T$  data. The authors would like to thank H. Belmouaddine for scientific insights, and G. Laliberté, P.-L. Karsenti, and the 3IT staff for technical support.

- 
- [1] L. Canham, *Handbook of Porous Silicon* (Springer, Berlin, 2014).
- [2] P. Azuelos, P. Girault, N. Lorrain, Y. Dumeige, L. Bodiou, L. Poffo, M. Guendouz, M. Thual, and J. Charrier, *J. Opt.* **20**, 085301 (2018).
- [3] H. F. Arrand, T. M. Benson, A. Loni, R. Arens-Fischer, M. Kruger, M. Thonissen, H. Luth, and S. Kershaw, *IEEE Photon. Technol. Lett.* **10**, 1467 (1998).
- [4] Y. Qu, L. Liao, Y. Li, H. Zhang, Y. Huang, and X. Duan, *Nano Lett.* **9**, 4539 (2009).
- [5] K. Kim and T. E. Murphy, *Opt. Express* **21**, 19488 (2013).
- [6] A. P. Cohn, W. R. Erwin, K. Share, L. Oakes, A. S. Westover, R. E. Carter, R. Bardhan, and C. L. Pint, *Nano Lett.* **15**, 2727 (2015).
- [7] B. González-Díaz, R. Guerrero-Lemus, P. Haro-González, D. Borchert, and C. Hernández-Rodríguez, *Thin Solid Films* **511-512**, 473 (2006).
- [8] L. Canham, *Appl. Phys. Lett.* **57**, 1046 (1990).
- [9] M. V. Wolkin, J. Jorne, P. M. Fauchet, G. Allan, and C. Delerue, *Phys. Rev. Lett.* **82**, 197 (1999).
- [10] C. Delerue, G. Allan, and M. Lannoo, *Phys. Rev. B* **48**, 11024 (1993).
- [11] W. J. Salcedo, F. J. R. Fernandez, and J. C. Rubim, *Spectrochim. Acta, Part A* **60**, 1065 (2004).
- [12] J. Sun, Y. W. Lu, X. W. Du, and S. A. Kulinich, *Appl. Phys. Lett.* **86**, 171905 (2005).
- [13] X.-W. Du, Y.-W. Lu, J.-P. Liu, and J. Sun, *Appl. Surf. Sci.* **252**, 4161 (2006).
- [14] A. R. Boucherif, A. Boucherif, G. Kolhatkar, A. Ruediger, and R. Arès, *Small* **13**, 1603269 (2017).
- [15] G. Kolhatkar, A. Boucherif, A. R. Boucherif, A. Dupuy, L. G. Fréchette, R. Arès, and A. Ruediger, *Nanotechnology* **29**, 145701 (2018).
- [16] L. V. Titova, T. L. Cocker, D. G. Cooke, X. Wang, A. Meldrum, and F. A. Hegmann, *Phys. Rev. B* **83**, 085403 (2011).
- [17] D. G. Cooke, A. N. MacDonald, A. Hryciw, J. Wang, Q. Li, A. Meldrum, and F. A. Hegmann, *Phys. Rev. B* **73**, 193311 (2006).
- [18] D. G. Cooke, A. Meldrum, and P. Uhd Jepsen, *Appl. Phys. Lett.* **101**, 211107 (2012).
- [19] W. He, A. Zakar, T. Roger, I. V. Yurkevich, and A. Kaplan, *Opt. Lett.* **40**, 3889 (2015).
- [20] M. Dovrat, Y. Goshen, J. Jedrzejewski, I. Balberg, and A. Sa'ar, *Phys. Rev. B* **69**, 155311 (2004).
- [21] W. Evers, J. Schins, M. Aerts, A. Kulkarni, P. Capiod, M. Berthe, B. Grandidier, C. Delerue, H. Van Der Zant, C. Van Overbeek, J. Peters, D. Vanmaekelbergh, and L. Siebbeles, *Nat. Commun.* **6**, 8195 (2015).
- [22] K. Židek, K. Zheng, C. Ponceca, M. Messing, L. Wallenberg, P. Chábera, M. Abdellah, V. Sundström, and T. Pullerits, *J. Am. Chem. Soc.* **134**, 12110 (2012).
- [23] A. Beaudoin, B. Salem, T. Baron, P. Gentile, and D. Morris, *Phys. Rev. B* **89**, 115316 (2014).
- [24] H. J. Joyce, C. J. Docherty, Q. Gao, H. H. Tan, C. Jagadish, J. Lloyd-Hughes, L. M. Herz, and M. B. Johnston, *Nanotechnology* **24**, 214006 (2013).
- [25] H. J. Joyce, J. L. Boland, C. L. Davies, S. A. Baig, and M. B. Johnston, *Semicond. Sci. Technol.* **31**, 103003 (2016).
- [26] D. Tsokkou, A. Othonos, and M. Zervos, *Appl. Phys. Lett.* **100**, 133101 (2012).
- [27] P. Parkinson, C. Dodson, H. Joyce, K. Bertness, N. Sanford, L. Herz, and M. Johnston, *Nano Lett.* **12**, 4600 (2012).
- [28] M. Li, G. Xing, G. Xing, B. Wu, T. Wu, X. Zhang, and T. C. Sum, *Phys. Rev. B* **87**, 115309 (2013).
- [29] R. Tomasiunas, I. Pelant, J. Kočka, P. Knápek, R. Lévy, P. Gilliot, J. B. Grun, and B. Hönerlage, *J. Appl. Phys.* **79**, 2481 (1996).
- [30] W. He, R. Wu, I. V. Yurkevich, L. T. Canham, and A. Kaplan, *Sci. Rep.* **8**, 17172 (2018).
- [31] J. Knab, X. Lu, F. Vallejo, G. Kumar, T. Murphy, and L. M. Hayden, *Opt. Mater. Express* **4**, 300 (2014).
- [32] A. Zakar, R. Wu, D. Chekulaev, V. Zerova, W. He, L. Canham, and A. Kaplan, *Phys. Rev. B* **97**, 155203 (2018).
- [33] R. Schwarz, F. Wang, M. Ben-Chorin, S. Grebner, A. Nikolov, and F. Koch, *Thin Solid Films* **255**, 23 (1995).
- [34] A. Cohn, A. Schimpf, C. Gunthardt, and D. Gamelin, *Nano Lett.* **13**, 1810 (2013).
- [35] H. Joyce, J. Wong-Leung, C.-K. Yong, C. Docherty, S. Paiman, Q. Gao, H. Tan, C. Jagadish, J. Lloyd-Hughes, L. Herz, and M. Johnston, *Nano Lett.* **12**, 5325 (2012).
- [36] G. M. Turner, M. C. Beard, and C. A. Schmuttenmaer, *J. Phys. Chem. B* **106**, 11716 (2002).



- [37] E. Hendry, M. Koeberg, B. O'Regan, and M. Bonn, *Nano Lett.* **6**, 755 (2006).
- [38] T. L. Cocker, D. Baillie, M. Buruma, L. V. Titova, R. D. Sydora, F. Marsiglio, and F. A. Hegmann, *Phys. Rev. B* **96**, 205439 (2017).
- [39] H. Němec, P. Kužel, and V. Sundström, *Phys. Rev. B* **79**, 115309 (2009).
- [40] P. Kužel and H. Němec, *Adv. Opt. Mater.* **8**, 1900623 (2020).
- [41] J. B. Baxter and C. A. Schmuttenmaer, *J. Phys. Chem. B* **110**, 25229 (2006).
- [42] M. R. Bergren, C. E. Kendrick, N. R. Neale, J. M. Redwing, R. T. Collins, T. E. Furtak, and M. C. Beard, *J. Phys. Chem. Lett.* **5**, 2050 (2014).
- [43] S. Heo, S. Yoon, S. Oh, D. Yoon, and H. Kim, *Nanoscale* **6**, 903 (2014).
- [44] L. V. Titova, T. L. Cocker, S. Xu, J.-M. Baribeau, X. Wu, D. J. Lockwood, and F. A. Hegmann, *Semicond. Sci. Technol.* **31**, 105017 (2016).
- [45] D. J. Jubgang Fandio, S. Sauze, A. Boucherif, R. Arès, and D. Morris, *Nanoscale Adv.* **2**, 340 (2020).
- [46] J. Strait, H. Wang, S. Shivaraman, V. Shields, M. Spencer, and F. Rana, *Nano Lett.* **11**, 4902 (2011).
- [47] F. Rana, J. H. Strait, H. Wang, and C. Manolatu, *Phys. Rev. B* **84**, 045437 (2011).
- [48] F. Rana, *Phys. Rev. B* **76**, 155431 (2007).
- [49] F. Rana, P. A. George, J. H. Strait, J. Dawlaty, S. Shivaraman, M. Chandrashekar, and M. G. Spencer, *Phys. Rev. B* **79**, 115447 (2009).
- [50] H. Němec, L. Fekete, F. Kadlec, P. Kužel, M. Martin, J. Mangeney, J. C. Delagnes, and P. Mounaix, *Phys. Rev. B* **78**, 235206 (2008).
- [51] Band structure and carrier concentration, silicon, <http://www.ioffe.ru/SVA/NSM/Semicond/Si/bandstr.html>.
- [52] M. A. Rafiq, Y. Tsuchiya, H. Mizuta, S. Oda, S. Uno, Z. A. K. Durrani, and W. I. Milne, *J. Appl. Phys.* **100**, 014303 (2006).
- [53] Z. Durrani and M. Rafiq, *Microelectron. Eng.* **86**, 456 (2009).
- [54] X. Zhou, K. Usami, M. A. Rafiq, Y. Tsuchiya, H. Mizuta, and S. Oda, *J. Appl. Phys.* **104**, 024518 (2008).